

# On the mesoscopic Eulerian formalism for the simulation of non-isothermal dilute turbulent two-phase flows

By J. Dombard<sup>†‡</sup> AND L. Selle<sup>†‡</sup>

We address the numerical simulation of particle-laden turbulent flows in the dilute regime, i.e., when the volume fraction of the dispersed phase is small. However, because of the potentially large density difference between the two phases, the dispersed phase may be significantly inertial and not exactly follow the carrier. For a dilute two-phase flow (typically a cloud of droplets or solid particles in a turbulent gaseous flow), there are at least two effects of inertia: (1) Preferential concentration can result in steep gradients in the number density of particules and (2) Because inertial particles have a large ‘memory’ time scale, two particles that are very close can have drastically different properties, i.e., velocity, size and temperature. These peculiar characteristics call for specific modeling strategies and raise additional problems for the numerical simulation of dilute two-phase flows. A series of test cases are presented to evaluate the performance and robustness of two numerical strategies, in particular one called the PSI scheme that ensures the positiveness of the number density. Then a particle-laden turbulent planar jet is computed to evaluate the importance of the uncorrelated heat flux in the mesoscopic formalism.

---

## 1. Introduction

Particle or droplet-laden turbulent flows are encountered in industrial processes as well as natural phenomena. The accuracy of their numerical simulation can have a positive impact on a broad range of applications such as engine performance, pollutant emission levels, weather and climate prediction, etc. In this two-phase flow regime, there are several modeling approaches that can be broadly divided in three categories: (1) the flow can be resolved all the way down to the scale of the particle; (2) the particles can be tracked individually and followed in a Lagrangian way; and (3) a statistical description can be used to derive Eulerian equations for the dispersed phase, which is represented as a continuous field. Quite obviously, option (1) is the most expensive and despite significant advances, (Menard *et al.* 2007; Desjardins *et al.* 2008) remains out of reach for most turbulent dilute flows because of the computational cost. Strategies (2) and (3) are now widely used techniques, but both modeling and computational issues remain. Most Lagrangian formulations for example assume that the particle is a point resulting in approximations for source terms to and from the dispersed phase. The computational burden of Lagrangian simulations is also roughly proportional to the number of particles, which necessitates additional modeling for some applications. However, this framework is particularly attuned for flows far from equilibrium where the dispersed-phase behavior strongly depends on boundary and initial conditions. Throughout the paper, we will

<sup>†</sup> Université de Toulouse; INPT, UPS; IMFT (Institut de Mécanique des Fluides de Toulouse); Allée Camille Soula, F-31400 Toulouse, France

<sup>‡</sup> CNRS; IMFT; F-31400 Toulouse, France

consider particles rather than droplets because we do not address cases where the evaporation process is significant. Nevertheless, the same rationale applies to droplets.

The objective of this work is to address the challenges specific to option (3): the Eulerian formulation. Being a statistical description, the obvious advantage to the Eulerian formulation is that its computational cost does not depend on the number of particles. It is also very easy to parallelize through domain decomposition. However, two weak points will be addressed in this paper:

(a) **Numerics:** Particles tend to be ejected from high-rotation regions and gathered in high-strain regions (Squires & Eaton 1991) so that preferential concentration occurs and strong gradients and very small-scale structures are generated in the number density of the dispersed phase. Because it is crucial that this quantity remains positive, specific numerics must be used.

(b) **Modeling:** The Eulerian equations should account for the fact that two nearby inertial particles may have uncorrelated properties. Following the work of Février *et al.* (2005) on the decomposition of the velocity field, we will address here the the topic of uncorrelated particle temperature. Indeed, the particle (or droplet) temperature may have a great influence on evaporation rates or chemical reaction rates.

In Sec. 2 the mesoscopic Eulerian formalism (MEF) is presented with the conservation equations and models for the uncorrelated contributions to momentum and heat fluxes. Section 3 will present the numerics and an assessment of their performance on several academic cases. Finally in Sec. 4 the modeling of the heat transfer to the dispersed phase will be addressed in the case of a temporal planar turbulent jet.

## 2. The Mesoscopic Eulerian Formalism

### 2.1. General presentation

The MEF was originally presented by Février *et al.* (2005). Using Direct Numerical Simulations (DNS), they observed that two arbitrarily-close particles may have drastically different velocities. In other words, the two-point correlation between particle velocities does not reach unity when the distance goes to zero ( c.f. their Fig. 3). Based on this observation, the cornerstone of the MEF is a statistical-average operator,  $\langle \bullet | \mathcal{H}_f \rangle$  that corresponds to the average over all particle realizations for a fixed carrier-fluid realization  $\mathcal{H}_f$ . This operator splits the particle velocity,  $u_p$ , in two contributions: a continuous, self-coherent velocity,  $\tilde{u}_p = \langle u_p | \mathcal{H}_f \rangle$ , shared by all particles called the mesoscopic field and a spatially uncorrelated contribution,  $\delta u_p$ , referred to as Random Uncorrelated Motion (RUM). One has

$$u_p(t) = \tilde{u}_p(x_p(t), t) + \delta u_p(t), \quad (2.1)$$

where  $x_p(t)$  is the position of the particle at time  $t$ . Similarly, one can decompose the particle temperature  $T_p$  into its mesoscopic ( $\tilde{T}_p$ ) and uncorrelated ( $\delta T_p$ ) components:

$$T_p(t) = \tilde{T}_p(x_p(t), t) + \delta T_p(t). \quad (2.2)$$

From the perspective of particle dynamics, it can be simply said that the mesoscopic velocity and temperature are related to the coupling with the carrier phase, through drag and heat transfer, and that the RUM is caused by the inertia of the particles. Indeed, because of inertial effects, two particles may get to neighboring locations with different trajectories and therefore different properties (velocity, temperature, etc.). Consequently, for particle dynamics, the ratio of the inertial and viscous time scales acting on the

particles is central for the evaluation of the relative importance of the mesoscopic and uncorrelated contributions. This ratio is the Stokes number,  $St$ , defined as

$$St = \frac{\tau_p}{\tau_f}, \quad (2.3)$$

where  $\tau_p$  is the particle relaxation time and  $\tau_f$  a time scale typical of the carrier phase. Using the particle thermal time scale  $\tau_\theta$ , a thermal Stokes number,  $St_\theta$ , may be also defined as

$$St_\theta = \frac{\tau_\theta}{\tau_f}. \quad (2.4)$$

In this work, we will use the following definitions:

$$\tau_p = \frac{\rho_p d_p^2}{18\mu}; \quad \tau_f = \frac{L}{u'}; \quad \tau_\theta = \frac{3}{2} \text{Pr} \frac{C_p}{C_f} \tau_p \quad (2.5)$$

where  $\rho_p$  is the particle density,  $d_p$  its diameter, and  $C_p$  its heat capacity. The fluid kinematic viscosity is  $\mu$  and its constant-pressure heat capacity denoted  $C_f$ . The Prandtl number of the carrier fluid is  $\text{Pr}$ . The velocity and length scales of the fluid ( $u'$  and  $L$ , respectively) are detailed in Sec. 4.1.

## 2.2. Governing equations

The set of Eulerian equations for a non-isothermal dilute particle flow in the mesoscopic formalism was derived by Masi (2010):

$$\frac{\partial \tilde{n}_p}{\partial t} + \frac{\partial \tilde{n}_p \tilde{u}_{p,j}}{\partial x_j} = 0, \quad (2.6)$$

$$\frac{\partial \tilde{n}_p \tilde{u}_{p,i}}{\partial t} + \frac{\partial \tilde{n}_p \tilde{u}_{p,i} \tilde{u}_{p,j}}{\partial x_j} = -\frac{\tilde{n}_p}{\tau_p} (\tilde{u}_{p,i} - u_{f,i}) - \frac{\partial \tilde{n}_p \delta R_{p,ij}}{\partial x_j}, \quad (2.7)$$

$$\frac{\partial \tilde{n}_p C_p \tilde{T}_p}{\partial t} + \frac{\partial \tilde{n}_p C_p \tilde{u}_{p,j} \tilde{T}_p}{\partial x_j} = -\frac{\tilde{n}_p C_p}{\tau_\theta} (\tilde{T}_p - T_f) - \frac{\partial \tilde{n}_p C_p \delta \Theta_{p,j}}{\partial x_j}, \quad (2.8)$$

where  $\tilde{n}_p$  is the particle number density and  $u_f$  and  $T_f$  the fluid velocity and temperature, respectively. There are two unclosed terms in these equations corresponding to the RUM velocity stress tensor  $\delta R_{p,ij}$  and the RUM heat flux  $\delta \Theta_{p,j}$  defined as

$$\delta R_{p,ij} = \langle \delta u_{p,i} \delta u_{p,j} | \mathcal{H}_f \rangle, \quad (2.9)$$

$$\delta \Theta_{p,j} = \langle \delta T_p \delta u_{p,j} | \mathcal{H}_f \rangle, \quad (2.10)$$

## 2.3. Models

The RUM velocity stress tensor is decomposed into its spherical and deviatoric parts as

$$\delta R_{p,ij} = \delta R_{p,ij}^* + \frac{2}{3} \delta \theta_p \delta_{ij}, \quad (2.11)$$

where  $\delta \theta_p = 1/2 \delta R_{p,kk}$  is the RUM kinetic energy. Following Simonin *et al.* (2002) and Kaufmann (2004), the deviatoric part  $\delta R_{p,ij}^*$  is modeled by a viscosity assumption:

$$\delta R_{p,ij}^* = -\nu_{p,RUM} \left( \frac{\partial \tilde{u}_{p,i}}{\partial x_j} + \frac{\partial \tilde{u}_{p,j}}{\partial x_i} - \frac{2}{3} \frac{\partial \tilde{u}_{p,k}}{\partial x_k} \delta_{ij} \right), \quad (2.12)$$

$$\nu_{p,RUM} = \frac{\tau_p}{3} \delta \theta_p \quad (2.13)$$

whereas a transport equation is solved for the RUM kinetic energy

$$\frac{\partial \tilde{n}_p \delta \theta_p}{\partial t} + \frac{\partial \tilde{n}_p \tilde{u}_{p,j} \delta \theta_p}{\partial x_j} = -2 \frac{\tilde{n}_p}{\tau_p} \delta \theta_p - \tilde{n}_p \delta R_{p,ij} \frac{\partial \tilde{u}_{p,i}}{\partial x_j} - \frac{1}{2} \frac{\partial \tilde{n}_p \delta Q_{p,ij}}{\partial x_j}. \quad (2.14)$$

The third-order velocity correlation  $\delta Q_{p,ijk} = \langle \delta u_{p,i} \delta u_{p,j} \delta u_{p,k} | \mathcal{H}_f \rangle$  in Eq. 2.14 is modeled as suggested by Kaufmann *et al.* (2008):

$$\delta Q_{p,ij} = -2 \kappa_{p,RUM} \frac{\partial \delta \theta_p}{\partial x_j}, \quad (2.15)$$

$$\kappa_{p,RUM} = \frac{5 \tau_p}{3} \delta \theta_p. \quad (2.16)$$

With this, Eq. 2.7 is closed so the last contribution to model is the RUM heat flux  $\delta \Theta_p$  in Eq. 2.8. For this work, it was decided to use as little additional modeling as possible for the RUM heat flux so we opted for a resolution of the conservation equations for  $\delta \Theta_p$  (Masi 2010):

$$\begin{aligned} \frac{\partial \tilde{n}_p C_p \delta \Theta_{p,i}}{\partial t} + \frac{\partial \tilde{n}_p C_p \tilde{u}_{p,j} \delta \Theta_{p,i}}{\partial x_j} &= -\tilde{n}_p C_p \left( \frac{1}{\tau_p} + \frac{1}{\tau_\theta} \right) \delta \Theta_{p,i} - \tilde{n}_p C_p \delta \Theta_{p,j} \frac{\partial \tilde{u}_{p,i}}{\partial x_j} \\ &\quad - \tilde{n}_p C_p \delta R_{p,ij} \frac{\partial \tilde{T}_p}{\partial x_j} - \frac{\partial \tilde{n}_p \delta \Delta_{p,ij}}{\partial x_j}, \end{aligned} \quad (2.17)$$

with the only assumption that the third-order contribution  $\delta \Delta_{p,ij} = \langle \delta u_{p,i} \delta u_{p,j} \delta T_p | \mathcal{H}_f \rangle$  could be neglected. This last assumption is solely based on pragmatism as we do not yet have models available for this term.

### 3. Solver and numerical strategies

Equations 2.6 to 2.8 are implemented in the solver AVBP developed by CERFACS and Institut Français du Pétrole. They are similar to the Navier-Stokes equations except that they are known to have an extremely high compressibility, which allows for the formation of very steep gradients and calls for specific numerical schemes. In the work of De Chaisemartin *et al.* (2008) and De Chaisemartin (2009), so-called kinetic schemes were successfully used to solve these equations. However, these schemes can not yet be derived in the three-dimensional unstructured cell-vertex formalism of AVBP so we opted for a different approach. Two strategies for handling the steep gradients in the dispersed phase will be considered: the use of a positive scheme called PSI (for Positive Streamwise Invariant) and the use of high-order centered schemes together with selective artificial viscosity.

#### 3.1. Numerics

The typical failure for a numerical integration of Eqs. 2.6-2.8 is that the number density  $\tilde{n}_p$  becomes negative. To overcome this difficulty, it was decided to test the PSI scheme, which was developed by Struijs (1994) and implemented in AVBP by Lamarque (2007). The PSI scheme corresponds to an upwind discretization and its main property of interest here is its intrinsic positivity. The other option investigated is to use the TTGC scheme (Colin & Rudgyard 2000) together with selective artificial viscosity. TTGC is a centered scheme, third-order in space and time, that has been very successful for the simulation of gaseous compressible flows, with and without combustion (Selle *et al.* 2004; Roux *et al.* 2005). In order to improve its robustness given the high compressibility of

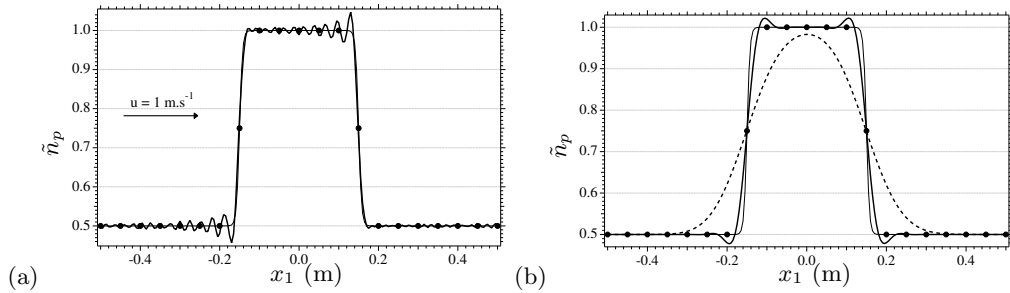


FIGURE 1. Particle number density for the one-dimensional convection test cases after one turnover time: (a) TTGC without artificial viscosity, (b) TTGC with artificial viscosity and PSI. —●— exact solution, — TTGC, - - - PSI.

the dispersed phase, artificial viscosity is added to the TTGC scheme. The procedure is too lengthy to be described in this report so the reader is referred to the work of Sanjosé (2009) (p. 90) for a thorough description. For both TTGC and PSI schemes, the integration of the carrier phase is performed using TTGC so that the differences in the results come only from the integration of the dispersed-phase equations (Eqs. 2.6, 2.7 2.8, 2.14 and 2.17).

### 3.2. Results

The first test case is the convection of a top-hat perturbation in the number density in a one-dimensional periodic domain of 1 m with 200 grid cells. The initial condition consists of a double hyperbolic tangent profile with an overall width of 0.3 m and a gradient width of 0.015 m. Figure 1 presents the results after one turnover time. Figure 1 (a) shows that the TTGC scheme generates spurious oscillations that are not acceptable. In Fig. 1 (b) TTGC is stabilized with artificial viscosity thus reducing the oscillations. One can also see that the PSI scheme preserves the positivity of the solution but the dissipation is substantial. The conclusion of this first test-case is that the TTGC scheme can be stabilized to overcome steep gradients and that the PSI scheme seems robust but its dissipation is too large.

Then a two-dimensional validation is carried out with the computation of a gaseous vortex, derived from a Gaussian potential, laden with an initially uniform field of particles. The gaseous phase is frozen and the objective is to accurately compute the formation of a dense ring of particles at the edge of the vortex caused by the ejection of the particles from the central region. The Eulerian simulations are compared to an analytical solution and to a Lagrangian computation. Figure 2 (a) compares the Lagrangian computation and the Eulerian using TTGC to the analytical solution. This solution is an exponential decay depending on the Stokes number of the particles and the turnover time,  $\tau_v$ , of the gaseous vortex. The agreement is excellent, despite a minor discrepancy for the Lagrangian simulation owing to the relatively small number of particles in the central cell. Figure 2 (b) is a radial cut of the particle number density at  $t/\tau_v = 100$ : one can see that the central region is void of particles and a dense ring has formed around the vortex. Both Eulerian computations with PSI and TTGC remain positive and accurately predict the location of the peak but its intensity is underestimated. The important conclusion of this test is that our numerics can represent preferential concentration but their robustness is achieved at the price of some dissipation as the peak in particle number density in the outer ring is missed by a factor of two. Interestingly, unlike in the one-dimensional test, PSI now has a better performance than TTGC.

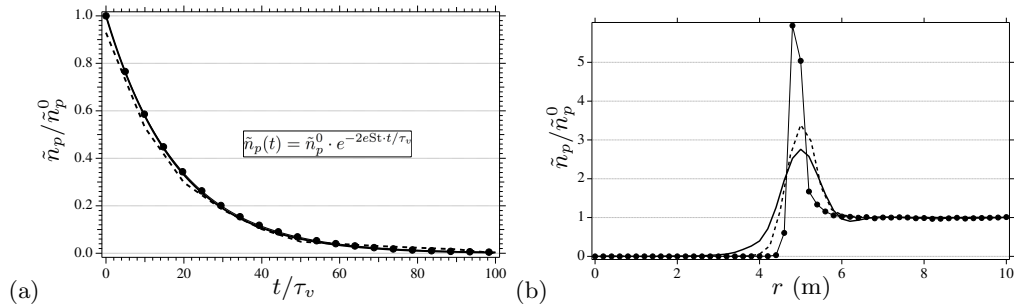


FIGURE 2. Validation on a two-dimensional vortex derived from a Gaussian potential. (a) Temporal evolution of the number density at the vortex center. (b) Radial profile of number density —●— Lagrangian, — TTGC, - - - PSI.

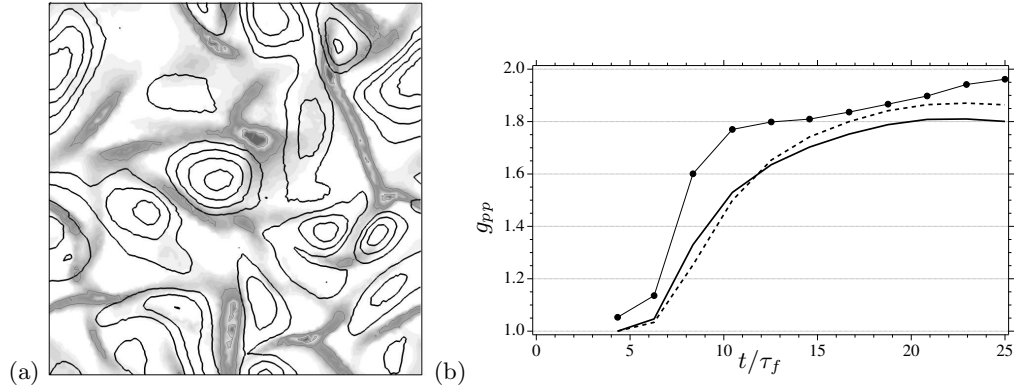


FIGURE 3. Validation on a three-dimensional particle-laden homogeneous isotropic turbulence. (a) Eulerian simulation with TTGC: vorticity isolines superimposed with gray shade of particle number density (dark = dense). (b) Particle segregation  $g_{pp} = \{\tilde{n}_p^2\} / \{\tilde{n}_p\}^2$ , ( $\{\bullet\}$  is the volume average over the whole domain) —●— Lagrangian, — TTGC, - - - PSI.

The final test is a particle-laden homogeneous isotropic turbulence at Reynolds number (based on the integral length scale)  $Re=17.76$ , Mach  $M=0.3$ , and  $St=0.55$  using a  $128^3$  mesh. This test includes the RUM and associated model for  $\delta R_{p,ij}$  described in Sec. 2.3, but there is no heat transfer. Figure 3 (a) shows how the particles are ejected from the center of the vortices, thus creating dense pockets with steep numbered-density gradients. This phenomenon called preferential concentration is measured by the quantity  $g_{pp} = \{\tilde{n}_p^2\} / \{\tilde{n}_p\}^2$ , where  $\{\bullet\}$  is the volume average over the whole domain. The temporal evolution of  $g_{pp}$  is presented in Fig. 3 (b). From an initially homogeneous field, the segregation starts at around  $t/\tau_v = 5$  and culminates at  $t/\tau_v = 20$ . Both TTGC and PSI schemes reach levels close to the Lagrangian reference, with a delay in the initial surge. For this most complex validation, both schemes have a comparable performance.

#### 4. Modeling heat transfer

In this section we address the simulation of non-isothermal dilute two-phase flows with the mesoscopic formalism described in Sec. 2. Based on the results of Sec. 3.2, it was decided to use the TTGC scheme for this computation.

---

Case name	Solver	RUM heat flux	Grid
NT_Lag_128	NTMIX	Yes	128 <sup>3</sup>
AV_Eul_128	AVBP	No	128 <sup>3</sup>
AV_Eul_128_HF	AVBP	Yes	128 <sup>3</sup>
AV_Eul_256	AVBP	No	256 <sup>3</sup>
AV_Eul_256_HF	AVBP	Yes	256 <sup>3</sup>

---

TABLE 1. List of cases, periodic boundary conditions.

#### 4.1. Configuration

The configuration is a temporal planar jet with the inner slab embedded with particles. The computational domain is a cubic box of size  $L_b = 2\pi 10^{-3}$  m, with periodic boundary conditions in all directions. The inner stream has a temperature  $T_f^{in} = 300$  K and velocity  $u_{f,1}^{in} = 0.15c$  (where  $c$  is the local speed of sound), whereas the outer region is initialized with  $T_f^{out} = 375$  K and  $u_{f,1}^{out} = 0$ . The thickness of the jet is  $L_{jet} = L_b/4$  and the transition with the outer region is achieved with a hyperbolic tangent function with an initial thickness  $\delta = L_{jet}/10$ . In order to favor the transition to turbulence, a perturbation is added to the initial velocity field. This perturbation is a synthetic homogeneous isotropic turbulence with a Passot-Pouquet spectrum. The most energetic length scale is  $L = L_{jet}/4$  and the turbulence intensity is  $u' = u_{f,1}^{in}/10$ . These values of  $L$  and  $u'$  are used to define the carrier time scale in Eq. 2.5. The initial particle temperature is  $T_p^0 = T_f^{in}$  and their initial velocity  $u_p^0 = u_f^{in}$ . Masi (2010) determined that this initial condition does not produce any artificial bias in the study of the dispersed phase after a simulation time of the order of  $3\tau_p$ . Dynamic and thermal Stokes number are respectively 0.46 and 2.

Four simulations of this configuration were performed with AVBP: two on a 128<sup>3</sup> mesh and two on a 256<sup>3</sup> mesh. For each mesh, the computation was performed with the MEF, both with and without uncorrelated heat-flux modeling (i.e., with and without Eq. 2.17). The first objective is to see the influence of Eq. 2.17 and the second goal is to match the reference Lagrangian simulation performed with NTMIX. The cases are summarized in Tab. 1.

#### 4.2. Results

It was first decided to duplicate in AVBP the Lagrangian simulation of NTMIX: however, the resolution of the Eulerian equations on the 128<sup>3</sup> did not seem to generate the steep number density gradients encountered in case NT\_Lag\_128. Through a discrete kinetic-energy balance, this was attributed to the excessive dissipation necessary to stabilize the numerics. The comparison of planar cuts of  $\tilde{n}_p$  are presented in Fig. 4 (a) for case AV\_Eul\_128 and in Fig. 4 (b) for case NT\_Lag\_128. One can see that the Eulerian computation does not generate the concentration levels encountered in the Lagrangian simulation. In order to reduce this dissipation, the Eulerian computations were conducted on a 256<sup>3</sup> mesh. The corresponding field of  $\tilde{n}_p$  presented in Fig. 4 (c) for case AV\_Eul\_256 shows much higher fluctuation levels. Moreover, on the 128<sup>3</sup> mesh, there was no noticeable difference between AV\_Eul\_128 and AV\_Eul\_128\_HF.

For a quantitative evaluation of the performance of the Eulerian formalism, plane-averaged quantities are now presented as a function of the cross-stream coordinate  $x_2$ . The mean of  $\tilde{n}_p$  is closely matched by all Eulerian simulations, as seen in Fig. 5 (a).

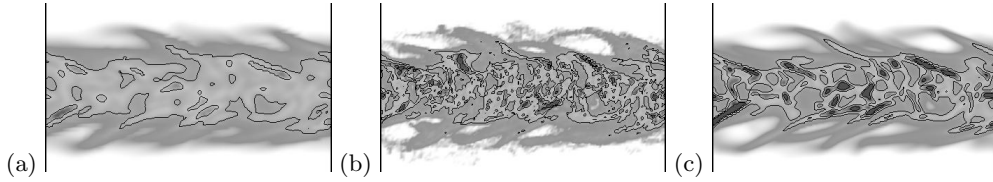


FIGURE 4. Planar cut of normalized number density  $\tilde{n}_p/\tilde{n}_p^0$ . The gray scale goes from 0 (white) to 2 (black). (a) AV\_Eul\_128; (b) NT\_Lag\_128; (c) AV\_Eul\_256\_HF.

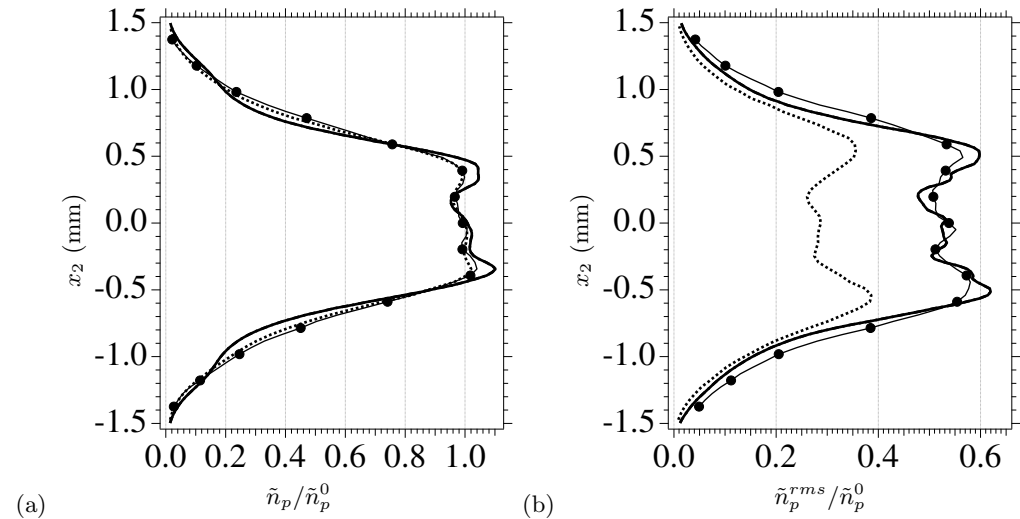


FIGURE 5. Homogeneous plane average: (a) normalized number density  $\tilde{n}_p/\tilde{n}_p^0$ ; (b) normalized rms of the number density  $\tilde{n}_p^{rms}/\tilde{n}_p^0$ . ---- AV\_Eul\_128; — AV\_Eul\_256\_HF; —●— NT\_Lag\_128.

The simulations with a better resolution have a slightly larger discrepancy. This will be discussed below. The rms of  $\tilde{n}_p$  is presented in Fig. 5 (b). Although the AV\_Eul\_128 clearly does not reach the levels encountered in the Lagrangian simulation, the predictions on the  $256^3$  closely match the reference. However, there is no noticeable difference between AV\_Eul\_256 and AV\_Eul\_256\_HF.

Then, because our interest is in heat-transfer modeling, the mean and rms particle temperatures are plotted in Fig. 6. The mesoscopic temperature  $\tilde{T}_p$  presented in Fig. 6 (a) is well reproduced for all computations. This kind of precision seems adequate for use in engineering applications. The rms of the temperature, plotted in Fig. 6 (b), is slightly under-predicted for case AV\_Eul\_128 and over-estimated in both  $256^3$  simulations. This over-estimation is suspected to be caused by the under-estimation of the RUM kinetic energy.

So far, we have compared only mean and rms mesoscopic quantities. These quantities are of interest from an engineering perspective, but they are also driven by higher-order correlations, namely the RUM kinetic energy  $\delta\theta_p$  and the RUM heat flux  $\delta\Theta_p$ . The RUM quantities not only impact the evolution of the mesoscopic variables, but they are key to other interactions such as particle collisions or droplet evaporation. Indeed, the uncorrelated fluctuation of velocity must be accounted for in the collision rate and similarly the uncorrelated temperature in the evaporation (or chemical reaction) rate. The RUM kinetic energy is presented in Fig. 7 (a) and it is obvious that none of the Eulerian

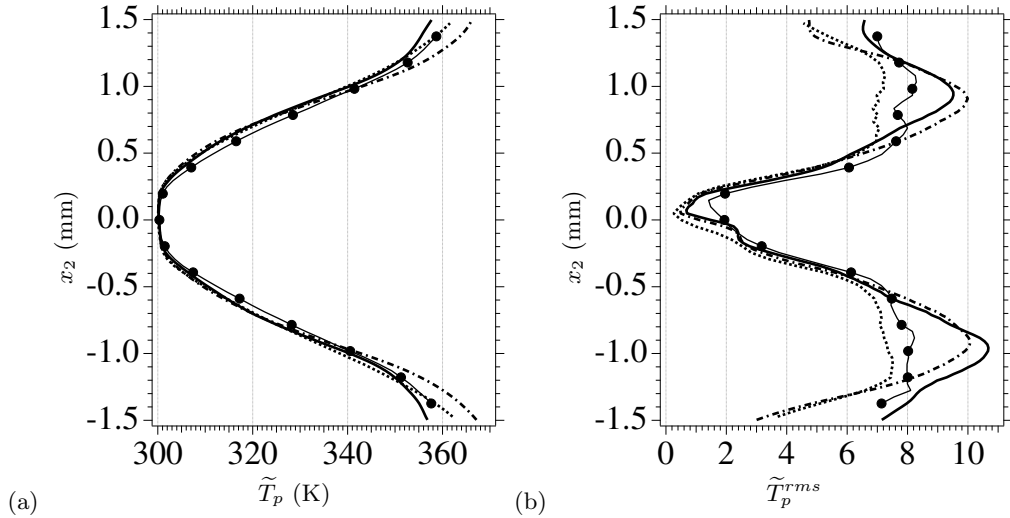


FIGURE 6. Mean (a) and rms (b) particle temperatures. --- AV\_Eul\_128; - - - AV\_Eul\_256; — AV\_Eul\_256\_HF; ●— NT\_Lag\_128.

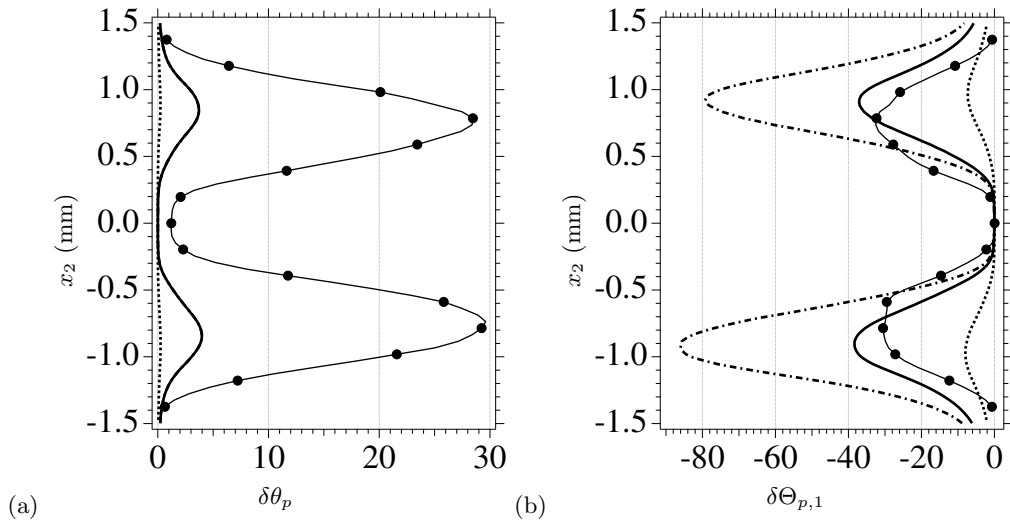


FIGURE 7. RUM kinetic energy (a) and streamwise component of the RUM heat flux (b). --- AV\_Eul\_128; - - - AV\_Eul\_256; — AV\_Eul\_256\_HF; ●— NT\_Lag\_128.

simulations predicts the correct level of  $\delta\theta_p$ , even though the  $256^3$  cases do a better job. The first-order impact of  $\delta\theta_p$  is on the momentum equation (c.f. Eq. 2.7), which then causes changes in the number density field through Eq. 2.6. One may then wonder how the profile of  $\tilde{n}_p$  for case AV\_Eul\_128 presented in Fig. 5 matches that of NT\_Lag\_128. The reason is that coincidentally, the excessive numerical dissipation, on average, does the job of the uncorrelated kinetic energy. For the  $256^3$  cases however, numerical dissipation is minimal, but  $\delta\theta_p$  is under-predicted, which leads to a stiffer averaged profile of  $\tilde{n}_p$ . Finally, the streamwise component of the RUM heat flux is presented in Fig. 7 (b). As expected, only the simulations on the  $128^3$  mesh under-predict  $\delta\Theta_{p,1}$  but case AV\_Eul\_256\_HF is in very good agreement with the Lagrangian reference. For case AV\_Eul\_256, Eq. 2.17

is solved, but  $\delta\Theta_p$  is set to zero in Eq. 2.8, which allows a sort of one-way evaluation of the RUM heat flux. It appears in Fig. 7 (b) that despite having similar mesoscopic quantities, in cases AV\_Eul\_256 and AV\_Eul\_256\_HF there is a factor two in the RUM heat flux indicating that the one-way evaluation of the RUM heat flux is inadequate.

## 5. Conclusion

Two numerical methods were tested for the computation of two-phase flows using an Eulerian set of equations. One is based on centered schemes with selective artificial dissipation whereas the other is a positive scheme called PSI. The performance of the two strategies is similar for two-dimensional and three-dimensional flows and the robustness of the PSI scheme makes it a good candidate for the computation of industrial configurations. The implementation of a higher-order version of PSI should further enhance its performance.

Direct Numerical Simulations of non-isothermal particle-laden flows were successfully conducted using the mesoscopic Eulerian formalism. It was shown that in the case of the planar temporal jet, the impact of the RUM heat flux on the mean quantities is moderate but its prediction is accurate. For a more accurate evaluation of the formalism, a more precise model is needed for the RUM kinetic energy because the levels predicted by the current viscosity assumption are too low, which affects the prediction of the mean quantities.

## Acknowledgments

The support of the Centre Informatique National de l'Enseignement Supérieur (CINES) for HPC resources under the allocation 2010-x2010026319 is gratefully acknowledged.

## REFERENCES

- COLIN, O. & RUDGYARD, M. 2000 Development of high-order Taylor-Galerkin schemes for unsteady calculations. *J. Comput. Phys.* **162** (2), 338–371.
- DE CHAISEMARTIN, S. 2009 Modèles eulériens et simulation numérique de la dispersion turbulente de brouillards qui s'évaporent. PhD thesis, Ecole Centrale de Paris, Chatenay-Malabry, France.
- DE CHAISEMARTIN, S., FRÉRET, L., KAH, D., LAURENT, F., FOX, R. O., RÉVEILLON, J. & MASSOT, M. 2008 Turbulent combustion of polydisperse evaporating sprays with droplets crossing: Eulerian modeling and validation in the infinite Knudsen limit. In *Proc. of the Summer Program*. Center for Turbulence Research, NASA Ames/Stanford Univ.
- DESJARDINS, O., MOUREAU, V. & PITSCH, H. 2008 An accurate conservative level set/ghost fluid method for simulating turbulent atomization. *J. Comput. Phys.* **227**, 8395–8416.
- FÉVRIER, P., SIMONIN, O. & SQUIRES, K. 2005 Partitioning of particle velocities in gas-solid turbulent flows into a continuous field and a spatially uncorrelated random distribution: Theoretical formalism and numerical study. *J. Fluid Mech.* **533**, 1–46.
- KAUFMANN, A. 2004 Vers la simulation des grandes échelles en formulation Euler/Euler des écoulements réactifs diphasiques. PhD thesis, INP Toulouse.
- KAUFMANN, A., MOREAU, M., SIMONIN, O. & HÉLIE, J. 2008 Comparison between

- lagrangian and mesoscopic eulerian modelling approaches for inertial particles suspended in decaying isotropic turbulence. *J. Comput. Phys.* **227** (13), 6448–6472.
- LAMARQUE, N. 2007 Schémas numériques et conditions limites pour la simulation aux grandes échelles de la combustion diphasique dans les foyers d'hélicoptère. PhD thesis, Institut National Polytechnique de Toulouse, France - Dynamique des Fluides.
- MASI, E. 2010 Theoretical and numerical study of the modeling of unsteady non-isothermal particle-laden turbulent flows by an eulerian-eulerian approach. PhD thesis, Institut National Polytechnique de Toulouse.
- MENARD, T., TANGUY, S. & BERLEMONT, A. 2007 Coupling level set/vof/ghost fluid methods: Validation and application to 3d simulation of the primary break-up of a liquid jet. *Int. J. Multiphase Flow* **33**, 510–524.
- ROUX, S., LARTIGUE, G., POINSOT, T., MEIER, U. & BÉRAT, C. 2005 Studies of mean and unsteady flow in a swirled combustor using experiments, acoustic analysis and large eddy simulations. *Combust. Flame* **141**, 40–54.
- SANJOSÉ, M. 2009 Evaluation de la méthode Euler-Euler pour la simulation aux grandes échelles des chambres à carburant liquide. PhD thesis, Institut National Polytechnique de Toulouse, France - Dynamique des Fluides.
- SELLE, L., LARTIGUE, G., POINSOT, T., KOCH, R., SCHILDMACHER, K.-U., KREBS, W., PRADE, B., KAUFMANN, P. & VEYNANTE, D. 2004 Compressible large-eddy simulation of turbulent combustion in complex geometry on unstructured meshes. *Combust. Flame* **137** (4), 489–505.
- SIMONIN, O., FEVRIER, P. & LAVIEVILLE, J. 2002 On the spatial distribution of heavy particle velocities in turbulent flow: from continuous field to particulate chaos. *J. Turb.* **3**.
- SQUIRES, K. D. & EATON, J. K. 1991 Preferential concentration of particles by turbulence. *Phys. Fluids* **3** (5), 1169–1178.
- STRUJIS, R. 1994 A multi-dimensional upwind discretization method for the euler equations on unstructured grids. PhD thesis, Technical University of Delft.